

<https://doi.org/10.1038/s44172-025-00518-y>

# Continuous tuning of ejector parameters via zeotropic component migration for optimising high-temperature heat pump

Check for updates

Zhengyong Li<sup>1,2,3</sup>, Youcai Liang<sup>1,2,3</sup> , Yan Zhu<sup>1,2,3</sup>, Shunchun Yao<sup>1,2,3</sup> & Zhibin Yu<sup>4</sup>

As the temperature lift increases, heat pump performance declines due to rising throttling losses in expansion valves. Ejectors present a promising alternative, enabling power recovery from the throttling process. However, fixed-geometry ejectors suffer performance degradation under off-design conditions. Here we propose leveraging the component migration characteristics of zeotropic refrigerants to continuously adjust critical ejector parameters by modulating the quality. This approach enables optimal performance across varying conditions without mechanical modifications. A vapor-injection heat pump cycle incorporating a component-adjustable ejector with three tunable parameters is developed. The concept of equivalent ejector efficiency was introduced, and the adjustment capability of typical high-temperature refrigerant mixtures was investigated, such as mixtures of butane (R600) and synthetic refrigerants (R245fa). Results show that, at a nominal heating capacity of 100 kW, R600/R245fa achieves a lower adjustable limit of  $-5\%$ , compared to  $-2\%$  for R1224yd(Z)/R1233zd(E) (synthetic refrigerant mixtures). These findings demonstrate the feasibility of efficient operation of fixed-geometry ejectors under variable conditions. The proposed system and regulation strategy offer a promising design alternative for industrial high-temperature heat pump applications.

Energy, as the cornerstone of human civilization, is undergoing a paradigm shift in supply models under carbon emission constraints. Extensive energy utilization has resulted in annual CO<sub>2</sub> emissions exceeding 12 billion metric tons<sup>1,2</sup>. Maintaining current emission trajectories would elevate the global average temperature by 6.1 °C by 2100, severely threatening ecosystem stability and sustainable development<sup>3</sup>. Notably, electricity generation and industrial processes contribute 67.4% of global carbon emissions, making decarbonization in these sectors essential for mitigating temperature rise and advancing sustainability<sup>4,5</sup>. Fossil fuel combustion in industrial boilers to meet the high-temperature heat demands of industrial processes results in the generation of large amounts of harmful gases such as CO<sub>2</sub> and SO<sub>2</sub>. Waste heat, an abundant byproduct in most industrial processes, is typically discharged directly into the environment. By implementing staged conversion and upgrading of waste heat with different temperatures, it is expected that recovering 40% of industrial waste heat<sup>6</sup>. High-temperature heat pumps can replace coal-fired boilers, consuming less than one-third of the primary energy of electric boilers, which is remarkable for decarbonizing

industrial process heating and achieving efficient electrification<sup>7,8</sup>. However, most industrial applications require high steam temperatures and large heating capacities, which conventional heat pumps cannot meet, and the cycle design, working fluid selection, and operational control of high-temperature heat pumps remain immature. Therefore, developing high-temperature heat pumps that meet industrial production demands is a key issue in reducing fossil fuel dependence and promoting decarbonization<sup>9</sup>.

The primary challenge in applying heat pump technology in high-temperature scenarios lies in the heat pump's compression process and refrigerant. High-temperature supply in industrial production processes leads to excessive compression ratios, reduced compression efficiency, and decreased heating capacity. Moreover, exceeding the compressor's discharge temperature limit may trigger thermal cracking of the lubricant, thereby increasing mechanical wear and the risk of failure. From a thermodynamic cycle perspective, conventional heat pump cycles are constrained by the limitations in compressor pressure ratio and elevated discharge temperatures. Vapor injection technology has been demonstrated

<sup>1</sup>School of Electric Power Engineering, South China University of Technology, Guangzhou, China. <sup>2</sup>Guangdong Province Engineering Research Center of High Efficient and Low Pollution Energy Conversion, Guangzhou, Guangdong, China. <sup>3</sup>Guangdong Province Key Laboratory of Efficient and Clean Energy Utilization, Guangzhou, China. <sup>4</sup>Department of Mechanical and Aerospace Engineering, University of Liverpool, Liverpool, UK. e-mail: [liangyoucai@scut.edu.cn](mailto:liangyoucai@scut.edu.cn); [Zhibin.yu@liverpool.ac.uk](mailto:Zhibin.yu@liverpool.ac.uk)

as an effective method to address insufficient heating capacity and overheating issues, with its efficacy manifested in reducing entropy generation during the compression process and enhancing refrigerant mass flow<sup>10,11</sup>. Large temperature differentials in conventional heat pump systems induce remarkable irreversible thermodynamic losses during the expansion process. Integrating components such as economizers, expanders, and ejectors can enhance thermodynamic performance. Among these, ejectors are particularly effective in mitigating irreversible losses and compression ratios, primarily by elevating compressor inlet pressure<sup>12</sup>. Despite the promising application prospects of vapor injection technology and ejectors, their practical implementation remains constrained by compressor material, structural, and control issues, as well as challenges related to the modeling and manufacturing of ejectors with two-phase characteristics.

According to existing research, vapor injection technology can be categorized into two types: sub-cooler vapor injection cycle (SVIC) and flash-tank vapor injection cycle (FVIC). Specifically, under design conditions, SVIC achieves peak  $COP_h$  and heating capacity improvements of 5.02% and 10.11%, respectively, compared to conventional heat pump cycles<sup>13</sup>. In contrast, FVIC demonstrates heating capacity and  $COP_h$  improvements over SVIC in the ranges of 3.2%–13.0% and 0.1%–18.2%, respectively<sup>14,15</sup>. Ejectors can be classified into constant-pressure mixing ejectors and constant-area mixing ejectors based on the nozzle position. The constant-area ejector has a theoretical advantage as it can accurately predict the actual performance of the ejector. However, when supersonic flow occurs, it is prone to choking phenomena<sup>16</sup>. For two-phase ejectors, internal condensation shocks do not exist, and the constant-area mixing model is more advantageous than the constant-pressure mixing model<sup>17</sup>. Fingas et al.<sup>18</sup> compared the performance of a throttling valve and a two-phase ejector as expansion devices. Experimental results showed that under identical operating conditions, the two-phase ejector exhibited a 38% performance improvement over the throttling valve. Vapor injection technology and ejectors, as two typical performance enhancement methods, play crucial roles in addressing issues such as heating capacity degradation, excessive discharge temperature, and high compression ratio. Mateu-Royo et al.<sup>19</sup> compared two heat pump systems employing an ejector and a parallel compression configuration (similar to vapor injection). The results showed that at a heating temperature of 140 °C, the  $COP_h$  and volumetric heating capacity of the parallel compression configuration increased by 36.5% and 44%, respectively, compared to the ejector-based system. Additionally, many researchers have combined ejectors with steam injection technology and added additional components to optimize the compression and expansion processes in heat pump cycles<sup>20,21</sup>. Compared to conventional cycles of single optimization measures, these improvements can achieve a  $COP_h$  enhancement of 7.7% ~ 36.6%.

Currently, the main factors affecting vapor injection are injection pressure and the superheat degree of the make-up gas. Existing studies have employed real-time control strategies such as extremum-seeking control and expansion valve stage control to address this issue<sup>22,23</sup>. A similar situation is that the low entrainment performance of the ejector and the narrow operating conditions limit the application of the ejector in practical scenarios<sup>24</sup>. The performance of ejectors is highly sensitive to structural parameters. When operating conditions deviate from the design point, the entrainment ratio remarkably decreases, potentially leading to complete failure of the entrainment effect<sup>25</sup>. Therefore, structurally adjustable ejectors are considered a viable solution for stabilizing system operation and expanding operational boundaries. Theoretically, by dynamically adjusting key geometric parameters such as primary nozzle position, area ratio (throat-to-mixing chamber diameter ratio), mixing chamber length, and convergence angle, the ejector can be optimized to achieve peak performance under current conditions<sup>26</sup>. Common adjustment methods include spindle regulation (via a conical plug in the nozzle throat), nozzle outlet position regulation (via axial displacement), and mixing chamber throat diameter modulation. These approaches dynamically reconfigure the nozzle and mixing chamber geometry, enabling adaptation to a broader range of

operating pressures and flow rates<sup>27</sup>. Compared to fixed-geometry ejectors, nozzle outlet position adjustment and adjustable spindle regulation demonstrate 16% and 400% performance improvements, respectively, under primary flow under-expansion conditions<sup>28</sup>. To achieve optimal geometric control of ejectors, Chen et al.<sup>29</sup> employed a subcooling control method to modulate the ejector throat area, achieving the highest entrainment ratio and reducing system power consumption by 6.99%, though the pressure ratio enhancement remained limited. In summary, adjustable-geometry ejectors exhibit advantages in energy efficiency and operational flexibility, yet face challenges including complex fluid dynamic design, leakage risks, and precision manufacturing requirements for dynamic components like spindles and nozzles.

Another challenge in the application of high-temperature heat pumps is the selection of suitable refrigerants. Existing literature indicates that the global warming potential (GWP) of HFC refrigerants is generally high, and they are currently being phased out. The flammability of HC refrigerants limits their widespread application, with the maximum allowable charge in commercial heat pump systems limited to 500 g<sup>30</sup>. HFO refrigerants have inherent chemical stability issues and can cause contamination of groundwater and soil. Wang et al.<sup>30</sup> believe that R718 offers high economic viability, safety, stability, critical temperature, vaporization latent heat, and operating performance, making it well-suited for high-temperature applications. However, compared to other refrigerants, R718 has a lower volumetric heating capacity, and its practical application still faces challenges such as oversized compressors and pressure corrosion issues, necessitating further development of steam compressor technologies<sup>31</sup>. To balance economic viability, environmental friendliness, and cycle performance, refrigerant mixtures with temperature glide characteristics are considered a potential optimal solution for high-temperature heat pumps<sup>32</sup>. Obika et al.<sup>33</sup> used a cyclohexane/cyclopropane mixture as a refrigerant in a traditional heat pump cycle. Under a temperature rise condition of 100 °C, the cycle  $COP_h$  of this mixture was 7.19% higher than that of the pure refrigerant (R1233zd(E)). The mixture refrigerant showed improvement in cycle performance. However, there are also studies that have shown the opposite results. Brodal et al.'s<sup>34</sup> research results indicate that in heat pump systems with ejectors, the cycle performance using blends of CO<sub>2</sub> and propane is inferior to that of pure refrigerants. This is because the mixing of substances is an irreversible entropy-increasing process, and using a refrigerant mixture may cause additional losses related to ejector efficiency or system heat exchange losses. This indicates that the composition and mixing ratio of the refrigerant mixture have a remarkable impact on its cycle performance. In addition, Ganesan et al.<sup>35</sup> introduced CO<sub>2</sub> into the high-pressure sub-cycle using butane and the low-pressure sub-cycle using pentane, respectively. Under a temperature lift of 70 °C and a CO<sub>2</sub> concentration of 5%, the cycle  $COP_h$  of the refrigerant mixture was improved by 20% compared to the original cascade system. To achieve a higher temperature lift, the CO<sub>2</sub> concentration in the mixture can be increased to 10%, at which point the cycle  $COP_h$  decreases by 16.6% compared to the original cascade system. This study indicates that differences in refrigerant type or composition between different sub-cycles in a cascade system can impact the overall system performance. At the same time, changes in the refrigerant mixture composition remarkably affect the effectiveness of the ejector and the compressor. Variations in the composition of the primary and secondary flows will lead to a shift in the ejector design point, while the dryness and composition at the gas-liquid separation point will determine the mass flow rate and state of the vapor injection<sup>36</sup>. Therefore, studying the refrigerant composition and the system's irreversibility losses is crucial for improving the cycle performance of refrigerant mixtures. In the aforementioned study, the performance of an ejector is typically represented by the entrainment ratio and the pressure lift ratio, which exhibit a certain trade-off and cannot accurately evaluate the ejector's capability in recovering expansion work. Elbel et al.<sup>37</sup> proposed the ejector efficiency, defined as the ratio of the actual recovered energy to the maximum obtainable power from the primary flow. Ejector efficiency performs well in assessing the efficiency of expansion work recovery; however, this literature does not provide further discussion on the

topic. Therefore, further research is needed on how to accurately and intuitively assess the performance of ejectors.

Based on the above discussion, in order to select appropriate refrigerant mixtures and enhance the performance of heat pump systems, this paper proposes two main innovations targeting the accurate assessment of ejector performance and the improvement of ejector adaptability: (1) a cycle equivalence analysis method; and (2) ejector optimization based on component migration. Their contributions lie in (1) clarifying the expansion work recovery mechanism of the ejector and the meaning of ejector efficiency; and (2) overcoming the issues of high implementation cost and structural complexity associated with adjustable ejectors. Specifically, the ejector can be regarded as an expander with a certain isentropic efficiency. On the other hand, by adjusting the dryness at the vapor-liquid separator inlet, the composition of the refrigerant mixture can be correspondingly adjusted. This operation allows the ejector to adapt to certain changes in operating conditions while maintaining a fixed structure, thereby expanding its working range and ultimately achieving the synergistic optimization of vapor injection and the ejector. The objective of this study is to accelerate the use of high-temperature heat pumps as a substitute for highly polluting boilers, ultimately enhancing the level of industrial electrification.

## Methods

### System description

Figure 1a–d illustrates the system diagrams and pressure–enthalpy (P–h) diagrams of a typical ejector-enhanced cycle and its equivalent cascade cycle, respectively. In this study, we further introduce the cycle equivalence analysis method in conjunction with these figures. As shown in Fig. 1a, the gas–liquid separator and the ejector achieve the separation and mixing of the working fluid, respectively. Specifically, in the ejector-enhanced cycle system, the two-phase ejector receives the fluid from the condenser outlet at point 3, expands it, and mixes it with the fluid from the evaporator outlet, with the final separation occurring in the gas–liquid separator. Figure 1c intuitively represents the functions of the two-phase ejector and gas–liquid separator shown in Fig. 1a. Unlike the traditional cascade heat pump, the high-pressure sub-cycle here uses an expander as the expansion device, with the recovered expansion work driving the compressor of the low-pressure sub-cycle. In comparison, the ejector is equivalent to the intermediate heat exchanger, expander, and low-stage compressor in the cascade cycle. Here, the isentropic efficiency of the expander during the expansion process is equal to the efficiency of the ejector. By employing the cycle equivalence method, the ejector-enhanced cycle is transformed into a cascade cycle, allowing the separation of refrigerant mixture components to be intuitively presented from the perspective of the cascade cycle. Meanwhile, this method provides a more intuitive interpretation of the abstract ejector efficiency, which is remarkable for assessing the actual expansion work recovery capability of the ejector and understanding the impact of non-azeotropic refrigerant composition changes.

Based on the equivalent analysis method, this study constructs a novel cycle with active composition regulation of zeotropic refrigerants, namely the flash-tank vapor injection heat pump cycle with a component-adjustable ejector (FVIC-CAE), as illustrated in Fig. 1e or Supplementary Note 1. This system integrates and modifies the conventional ejector-enhanced compression cycle with the flash-tank vapor injection cycle to adapt it to high-temperature operating conditions. After heat rejection in the condenser, the saturated liquid (Point 3) is divided into two streams. One stream undergoes pressure reduction through expansion valve 3 before entering gas–liquid separator 1 (Point 4). The other stream enters gas–liquid separator 1, where it releases heat and becomes subcooled (Point 6) before serving as the primary flow in the ejector. The fluid entering the gas–liquid separator 1 (Point 4) absorbs the heat released from the subcooled stream, increasing its vapor quality (Point 5) and undergoing phase separation. The separated vapor-phase fluid (5 g) is injected into the compressor, while the liquid-phase fluid (5 l) enters the intermediate heat exchanger, where it releases heat and becomes subcooled (Point 11). The subcooled liquid then

undergoes pressure reduction through expansion valve 2 (Point 12) before entering gas–liquid separator 2, where it is mixed at constant pressure with the ejector outlet fluid (Point 9), reducing the vapor quality in gas–liquid separator 2 (Point 10). After passing through gas–liquid separator 2, the fluid (Point 10) undergoes phase separation. The liquid-phase fluid (Point 10 l) is further expanded through expansion valve 1 (Point 13) and enters the evaporator, where it absorbs heat and evaporates into a gaseous state (Point 14). The resulting vapor is subsequently entrained by the primary flow. Meanwhile, the vapor-phase fluid (Point 10 g) enters the intermediate heat exchanger, where it absorbs the subcooling heat released by the liquid-phase fluid (5 l) from gas–liquid separator 1, becoming superheated (Point 1). The superheated fluid (Point 1) then enters the low-pressure chamber of the compressor, where it undergoes the first stage of compression (Point 15). The compressed fluid is mixed with the intermediate vapor injection (5 g), cooled to an intermediate state (Point 16), and then undergoes the second stage of compression in the high-pressure chamber of the compressor (Point 2). The high-temperature, high-pressure vapor then enters the condenser, where it releases heat and condenses into liquid (Point 3), thereby completing the cycle.

The cycle described in this study exhibits the following design characteristics: (1) In conventional regenerative cycles, superheat from subcooling is directly utilized to heat the compressor inlet fluid. The large heat exchange temperature difference results in remarkable irreversible heat transfer losses. In contrast, this study adopts a stepwise subcooling heat exchange approach, where the high-pressure stage subcooling heat is released to the medium-pressure stage, and the medium-pressure stage subcooling heat is used to superheat the compressor inlet fluid, thereby reducing heat exchange losses. (2) At present, most commonly used high-temperature refrigerants have a saturated vapor line with a positive slope (As shown in Fig. 4a). In conventional flash-tank vapor injection cycles, the vapor quality at the flash separation point is relatively low, leading to a lower mass flow rate of injected vapor and a limited  $COP_h$  improvement. This system utilizes subcooling heat to heat the flash tank, increasing the separation vapor quality and overcoming the issue of low vapor quality in vapor injection with high-temperature refrigerants. (3) Three possible pathways exist for the high-temperature, high-pressure fluid at the condenser outlet. The first fluid stream utilizes thermal energy via subcooling and pressure energy via the ejector. The second and third fluid streams undergo throttling and heat absorption in expansion valve 3, after which they are separated. The second stream serves as the supplementary refrigerant for the compressor, reusing its pressure and thermal energy. The third stream undergoes subcooling in the intermediate heat exchanger and ultimately flows toward the evaporator. The pressure reduction process from the condenser outlet to the evaporator inlet adopts staged expansion, minimizing irreversible losses. (4) This cycle does not make remarkable alterations to the traditional ejector-compressor cycle or vapor injection superheating cycle, allowing it to meet the needs of high-temperature heat pumps with relatively simple piping. It effectively reduces the exhaust temperature and compressor pressure ratio, while enhancing the heat supply and meeting the superheating requirements of refrigerants with high critical temperatures<sup>38</sup>. Although this paper introduces innovations in the cycle structure, it also focuses on using vapor quality regulation to alter the composition of the primary and secondary flows in the ejector, ultimately achieving effective operation of the ejector with a fixed structure under varying operating conditions.

### Ejector model

This paper uses a constant-area mixing model to simulate the two-phase ejector in the system, considering the impact of its structural parameters while calculating the thermodynamic properties of the internal fluid. Therefore, the ejector model here is divided into a thermodynamic model and a structural design model. To simplify the calculations, the following assumptions are made for the constructed ejector model:

(1) The velocities of the fluid entering and leaving the ejector are neglected.

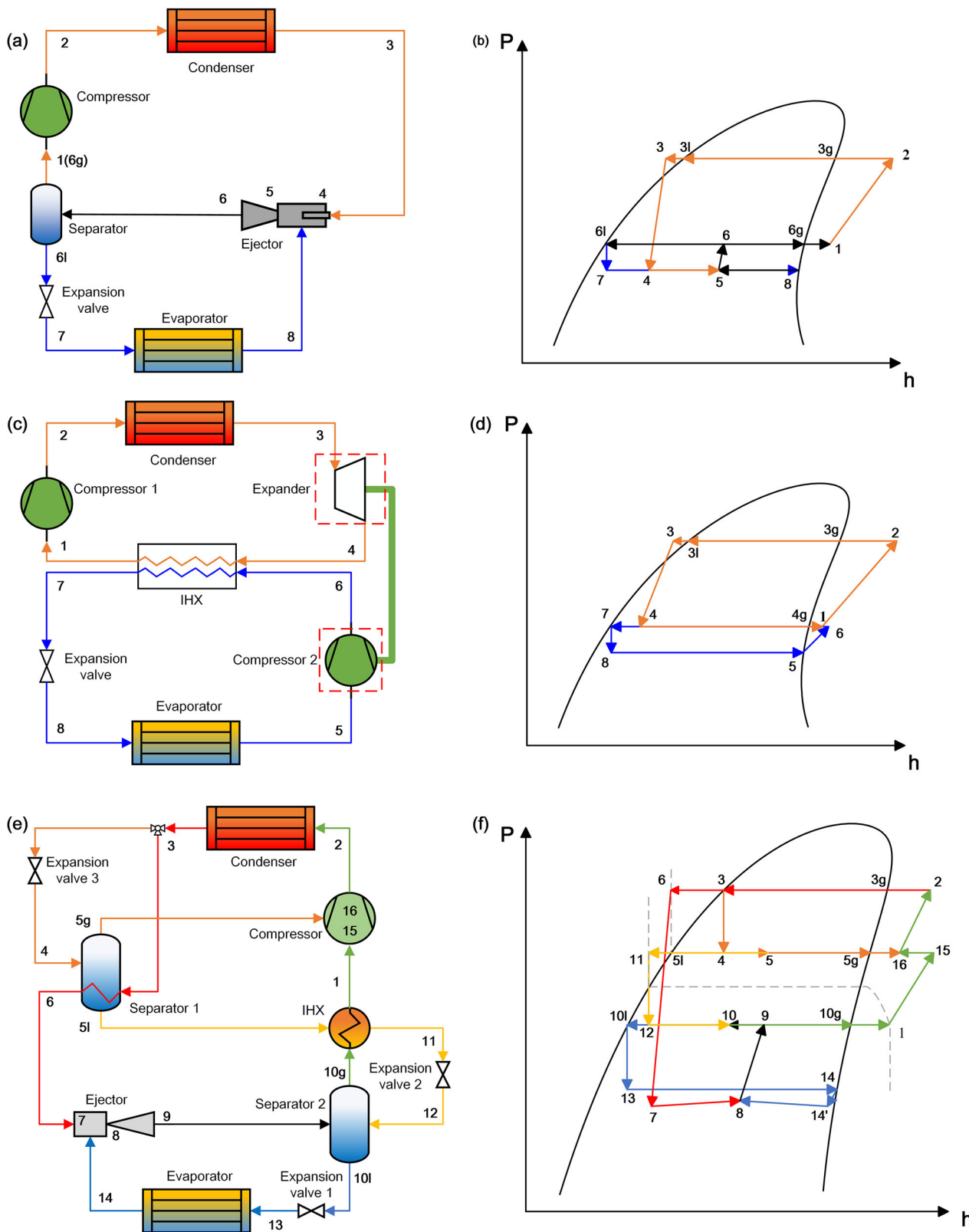


**Fig. 1 | System and pressure–enthalpy diagram.** **a** Ejecter enhanced heat pump cycle; **b** corresponding P–h diagram; **c** equivalent cascade cycle, **d** corresponding P–h diagram; **e** Flash-tank vapor injection heat pumps cycle with a component-adjustable ejector (FVIC-CAE); **f** corresponding P–h diagram.

- (2) The fluid flow outside the mixing chamber in the ejector is assumed to be one-dimensional and uniform.
- (3) The losses within the ejector are approximated by an isentropic efficiency.
- (4) Heat exchange between the ejector and the external environment is neglected.
- (5) The pressures of the primary and secondary flows at the interface at the inlet of the mixing chamber are assumed to be equal.

**Table 1 | Thermodynamic model of ejector<sup>17</sup>**

Parameter	Formula	Auxiliary
Pressure lift ratio	$r_p = P_9/P_{14}$	(6)
Definition of entrainment ratio	$\mu = m_{gt}/m_{pf}$	(7)
Nozzle		
Outlet enthalpy of the nozzle	$h_7 = h_6 - \eta_n(h_6 - h_{7, is})$	(8) $\eta_n = 0.85$ (9)
Outlet velocity of the nozzle	$u_7 = \sqrt{2(h_6 - h_7)}$	(10)
Outlet cross-sectional area of the nozzle	$A_7 = \frac{m_p}{\rho_7 u_7}$	(11)
Suction chamber		
Pressure of the suction chamber	$P_{14'} = P_7$	(12)
Enthalpy of the suction chamber	$h_{14'} = h_{14} - \eta_s(h_{14} - h_{14', is})$	(13) $\eta_s = 0.85$ (14)
Cross-sectional area of the suction chamber	$A_{14'} = \frac{\mu m_p}{\rho_{14'} u_{14'}}$	(15)
Mixing chamber		
Cross-sectional area of the mixing chamber	$A_8 = A_7 + A_{14'}$	(16)
Mass conservation equation	$m_p(1 + \mu) = \rho_8 u_8 A_8$	(17)
Momentum theorem	$u_7 + \mu u_{14'} + P_7 A_8 = u_8(1 + \mu) \left(1 + \frac{f_m}{2d}\right) + P_8 A_8$	(18)
Energy conservation equation	$h_6 + \mu h_{14} = (1 + \mu)(h_8 + \frac{1}{2}u_8^2)$	(19)
Coefficient of friction resistance	$\frac{1}{\sqrt{f_m}} = 2 \lg(\text{Re} \sqrt{f_m}) - 0.8$	(20) $\text{Re} = \frac{u_8 d \rho_8}{\mu_{v,8}}$ (21)
Outlet velocity of the mixing chamber	$\rho_8 u_8 = \rho_{8'} u_{8'}$	(22) $u_{8'} = u_8$ (No shock wave) (23)
Outlet pressure of the mixing chamber	$\rho_8 u_8^2 + P_8 = \rho_{8'} u_{8'}^2 + P_{8'}$	(24) $P_{8'} = P_8$ (No shock wave) (25)
Outlet enthalpy of the mixing chamber	$h_8 + \frac{1}{2}u_8^2 = h_{8'} + \frac{1}{2}u_{8'}^2$	(26) $h_{8'} = h_8$ (No shock wave) (27)
Diffuser		
Outlet enthalpy of the diffuser	$h_9 = h_{8'} + \frac{u_{8'}^2}{2}$	(28) $\eta_d = 0.85$ (29)
Outlet enthalpy of the diffuser	$P_9 = f(h_{8', is}, s_{8'})$	(30) $h_{8', is} = h_{8'} + \eta_d(h_9 - h_{8'})$ (31)

$\mu_{v,8}$  is the dynamic viscosity of point 8.

The thermodynamic parameter equations for each component of the two-phase ejector are summarized in Table 1. When the fully mixed fluid velocity at the mixing chamber exit exceeds the speed of sound, it indicates the onset of shockwaves, and the post-shock fluid state is denoted as 8'. The speed of sound in a two-phase gas-liquid flow can be calculated using the following equation:

$$\alpha_v = \frac{1}{1 + \frac{1-x}{x} \frac{\rho_v}{\rho_l}} \tag{1}$$

$$c = \sqrt{kR_g T \left( \alpha_v^2 + \alpha_v(1 - \alpha_v) \frac{\rho_l}{\rho_v} \right)^{-1}} \tag{2}$$

Building upon the established thermodynamic model of the ejector, the critical structural parameters of the ejector are calculated. Due to the metastable phenomenon occurring in the liquid-phase primary flow of the two-phase ejector during rapid depressurization (serving as an expansion device), this study employs the Henry-Fauske model that incorporates non-equilibrium metastable effects<sup>39</sup>. The formulas for calculating the critical pressure  $P_{cr}$  and critical mass flux  $G_{cr}$  are derived as follows:

$$G_{cr} = \sqrt{\left( \left( (v_{gt} - v_6) \frac{N}{s_{gt} - s_{lt}} \frac{d(s_{lt})}{d(P)} \right)_t \right)^{-1}} \tag{3}$$

$$P_{cr} = P_6 - \frac{v_6 G_{cr}^2}{2} \tag{4}$$

$$N = \begin{cases} \frac{s_6 - s_{lt}}{0.14(s_{gt} - s_{lt})}, & x < 0.14 \\ 1, & x \geq 0.14 \end{cases} \tag{5}$$

Where  $v_6$  and  $s_6$  represent the specific volume and specific entropy of the working fluid at the primary nozzle inlet, respectively;  $v_{gt}$  and  $s_{gt}$  denote the specific volume and entropy of the vapor phase at the nozzle throat, while  $v_{lt}$  and  $s_{lt}$  correspond to the liquid phase at the throat. The units for specific enthalpy and entropy are m3 K-1 and kj kg-1 K-1, respectively.

The ejector structural design model involves equations summarized in Table 2.

It is noteworthy that if  $P_7 \leq P_{cr}$ , a convergent-divergent (Laval) nozzle must be selected for the primary nozzle, necessitating additional calculations for the throat diameter. Conversely, if  $P_7 > P_{cr}$ , a convergent nozzle suffices, where the exit diameter of the convergent-divergent nozzle is equivalent to its throat diameter.

**System model**

This study performs an energy analysis of the components of the described system based on the mass conservation and energy conservation equations, and combines the second law of thermodynamics to analyze the relevant energy parameters of each component. To simplify the analysis, the following assumptions are made for the system model:

- (1) The heat loss, flow friction, and pressure drop in the system are neglected.
- (2) The system operates under steady-state conditions, with no consideration of transient effects on the system.
- (3) The isentropic efficiency of the compressor is linearly related to the pressure ratio.

- (4) The vapor-liquid separator has ideal separation efficiency, achieving complete separation of vapor and liquid.
- (5) The temperature difference at each pinch point in the system is assumed to be 5 °C.

The heating coefficient of performance ( $COP_h$ ) of the system can be calculated using the following equation:

$$COP_h = \frac{Q_{con}}{W_{com}} \quad (43)$$

The isentropic efficiency of the compressor can be calculated using the following equation<sup>40</sup>:

$$\eta_{com} = 0.85 - 0.0467r_c \quad (44)$$

$$r_c = \frac{P_{com,out}}{P_{com,in}} \quad (45)$$

**Table 2 | Structural design model of ejector<sup>17,39</sup>**

Parameter	Formula
Nozzle	
Outlet diameter of the nozzle	$D_{no} = \sqrt{\frac{4m_p}{\pi p_7 \sqrt{2(h_6 - h_7)}}}$ (32)
Diameter of the nozzle throat	$D_{nt} = \sqrt{\frac{4m_2}{\pi G_{cr}}}$ (33)
Length of the nozzle narrowing segment	$L_{nn} = \frac{D_6 - D_{nt}}{2 \tan(\theta_{nn})}$ (34)
Length of the nozzle expansion segment	$L_{ne} = \frac{D_7 - D_{nt}}{2 \tan(\theta_{ne})}$ (35)
Angle of the nozzle narrowing segment	$\theta_{nn} = 36^{\circ 41}$ (36)
Angle of the nozzle expansion segment	$\theta_{ne} = 3^{\circ 41}$ (37)
Suction chamber	
Area of the suction chamber	$A_s = 8A_{no}$ (38)
Angle of the suction chamber narrowing segment	$\theta_s = 45^{\circ 42}$ (39)
Length of the mixing chamber	$L_m = 10D_m$ (40)
Diffuser	
Length of the diffuser	$L_d = \frac{D_9 - D_m}{2 \tan(\frac{\theta_d}{2})}$ (41)
Angle of the diffuser	$\theta_d = 7^{\circ 43}$ (42)

The ratio of flow splitting of the system can be calculated by the following equation:

$$\varepsilon = \frac{m_4}{m_2} \quad (46)$$

The ambient temperature and pressure are 25 °C and 101 kPa, respectively.

The mass conservation equations and energy conservation equations calculation formulas for components within the system are summarized in Table 3.

**Equivalent cascade method**

This study approximates the ejector-enhanced cycle to a cascade cycle. The following assumptions are made for the application of the equivalent method:

- (1) In the equivalent cascade cycle, isothermal heat transfer occurs in the intermediate heat exchangers.
- (2) The isentropic efficiency of compressor 2 is calculated using the same formula as for compressor 1.
- (3) The intermediate temperature of the equivalent cascade cycle is assumed to be the same as the temperature of the fluid at the ejector outlet.
- (4) The isentropic efficiency of the expander is not a fixed value as in the traditional case.

For the equivalent cascade cycle, the actual power output of the expander is equal to the power consumed by the hypothetical compressor 2. Therefore, the isentropic efficiency of this expander can be calculated by the following formula:

$$\eta_{expander} = \frac{W_{com2}}{m_1(h_3 - h_{4,is})} = \frac{m_8(h_6 - h_5)}{m_1(h_3 - h_{4,is})} = \eta_{eje} \quad (47)$$

The equivalent coefficient of performance ( $COP_{h,e}$ ) is calculated as:

$$COP_{h,e} = \frac{Q_{con}}{W_{com1}} \quad (48)$$

For the ejector-enhanced cycle, the overall performance of the ejector within the system can be evaluated using the ejector efficiency, which is

**Table 3 | Equations for the conservation of mass and energy of the components of the system, and the formula for the destruction of exergy<sup>44</sup>**

Components	The conservation of mass equation	The conservation of energy equation
Compressor	$m_1 + m_{5g} = m_2$ (50)	$W_{com} = m_1(h_{15} - h_1) + (m_1 + m_{5g})(h_2 - h_{16})$ (51)
Separator 1	$m_4 + m_{3,6} = m_{5g} + m_{5l} + m_6$ (52)	$m_4h_4 + m_{3,6}h_3 = m_{5g}h_{5g} + m_{5l}h_{5l} + m_6h_6$ (53)
Separator 2	$m_{12} + m_9 = m_{10g} + m_{10l}$ (54)	$m_9h_9 + m_{12}h_{12} = m_{10g}h_{10g}$ (55)
Expansion valve 1	$m_{10l} = m_{13}$ (56)	$m_{10l}h_{10l} = m_{13}h_{13}$ (57)
Expansion valve 2	$m_{11} = m_{12}$ (58)	$m_{11}h_{11} = m_{12}h_{12}$ (59)
Expansion valve 3	$m_{3,4} = m_4$ (60)	$m_{3,4}h_3 = m_4h_4$ (61)
Condenser	$m_2 = m_3$ (62)	$Q_{con} = m_2(h_2 - h_3)$ (63)
Evaporator	$m_{13} = m_{14}$ (64)	$Q_{eva} = m_{13}(h_{14} - h_{13})$ (65)
Ejector	$m_6 + m_{14} = m_9$ (66)	See Table 1
IHX	$m_{10g} + m_{5l} = m_1 + m_{11}$ (67)	$m_{10g}h_{10g} + m_{5l}h_{5l} = m_1h_1 + m_{11}h_{11}$ (68)

calculated as<sup>37</sup>:

$$\eta_{je} = \frac{m_{sf}(h(P_9, s_{14}) - h_{14})}{m_{pf}(h_6 - h(P_9, s_6))} = \eta_{expander} \quad (49)$$

The calculations for the other components are the same as those in Section 3.2 of the system model.

The equivalent cascade system intuitively presents the role of the ejector as an expansion device and completely separates the gas-phase and liquid-phase fluids at the outlet of the vapor-liquid separator into two distinct streams. The compositional differences between the gas and liquid phases of the zeotropic refrigerant are thereby transformed into the refrigerant differences between the high-pressure and low-pressure sub-cycles in the cascade cycle.

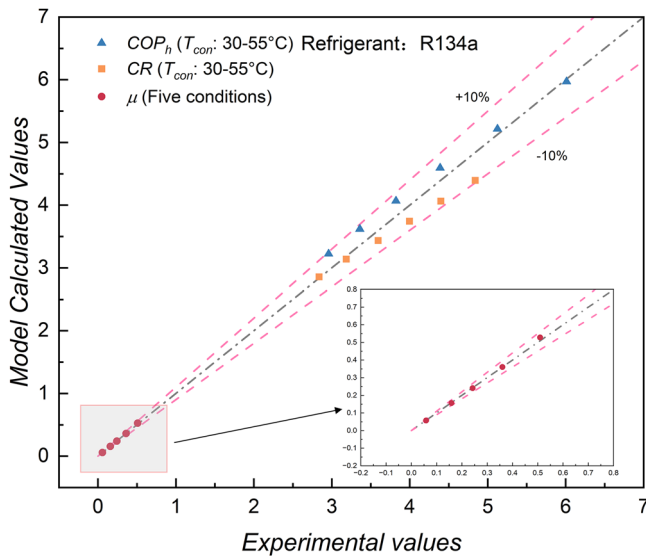


**Fig. 2 | Ejector and system thermodynamic model validation<sup>17</sup>.** In the model verification of this paper, the ejector coefficient, the compression ratio of the compressor, and the system performance coefficient were used as verification indicators, and the errors of all of them exceeded 10%.

**Table 4 | Structural design model validation of the ejector**

	$D_{nt}/mm$	$D_{no}/mm$	$D_m/mm$	$L_m/mm$	$L_d/mm$
Ref. <sup>23</sup>	1.86	4.60	10.00	100.00	49.00
Calculated	1.59	4.64	9.92	99.15	49.74
Error	14.5%	0.9%	0.8%	0.85%	1.51%

**Table 5 | The boundary conditions in ref. 17**

Parameters	Case 1	Case 2	Case 3	Case 4	Case 5
Condenser outlet temperature (°C)	48.70	48.80	48.70	48.20	48.00
Outlet subcooling of condenser (°C)	2.90	3.30	4.00	4.70	5.10
Inlet temperature of LT evaporator (°C)	-1.60	1.00	3.10	4.90	7.20
Outlet superheat of LT evaporator (°C)	23.90	20.90	18.60	16.40	13.30
Cooling capacity of HT evaporators (kW)	1.93	1.85	1.79	1.72	1.61
Cooling capacity of LT evaporators (kW)	0.12	0.32	0.48	0.69	0.91
Refrigerant	R134a	R134a	R134a	R134a	R134a

**Model validation**

To ensure the accuracy of the ejector model used in this study, the constant-area mixing thermodynamic model and the structural design model of the ejector are respectively validated. The validation results are shown in Fig. 2 and Table 4. As shown in Fig. 2, under the five boundary conditions as shown in Table 5<sup>17</sup>, the maximum error of the ejector entrainment ratio under five different boundary conditions is only 3.5%, and the minimum error is less than 0.01%. The ejector thermodynamic model adopted in this study can maintain low errors under varying boundary conditions, demonstrating the validity of the model. In addition, when the condensation temperature of the system gradually increases from 30 °C to 55 °C, both the coefficient of performance ( $COP_h$ ) and the compression ratio (CR) will continue to rise (cooling capacity ratio:1.5,  $T_{eva,l} = -5$  °C, without subcooling and superheating, refrigerant: R134a). As shown in Fig. 2, the model used in this study shows good agreement with the reference values, with maximum errors of 8.91% and 9.17% for  $COP_h$  and CR, respectively, further verifying the effectiveness of the constant-area mixing thermodynamic model.

For the ejector design model, the structural parameters of the ejector are calculated under the boundary conditions of a condensation temperature of 40 °C, refrigerant of R134a, subcooling degree of 5 °C, evaporation temperature of -5 °C, superheat degree of 7 °C, total cooling capacity of 15 kW, and a cooling load ratio of 1.5. According to Table 4, except for the nozzle throat diameter, the calculated dimensions of other ejector components show good agreement with the reference values. Although the error in the calculation of the nozzle throat diameter is 14.5%, the absolute deviation is only 0.27 mm. This small-scale characteristic leads to an amplified percentage error. In actual manufacturing, the error in the structural design model of the ejector remains within an acceptable range. The calculations in this study are conducted using MATLAB and REFPROP 10.0, and the overall model computation flowchart is shown in Fig. 3.

**Results and discussion**

**Analysis of refrigerants**

In high-temperature applications, the selection of heat pump working fluids is constrained by their critical temperatures, further narrowing the range of environmentally friendly refrigerants available. To explore environmentally friendly refrigerants suitable for high-temperature applications and component regulation, preliminary calculations were conducted for the high-temperature refrigerants listed in Table 6. To make the system applicable to most common industrial scenarios, the typical operating conditions in this study are as follows: an evaporation temperature of 50 °C, a condensation temperature of 125 °C, a heating capacity of 100 kW, an Initial component of refrigerant of 0.5, and a flow splitting ratio of 0.5. These refrigerants were then mixed to form refrigerant mixtures, and their performance is illustrated in Fig. 4b. As can be seen from the figure, the highest  $COP_h$  (3.39) occurs at (R4, R4), while the lowest  $COP_h$  (2.47) occurs at the combination of (R1, R9). Selecting the refrigerant with the best performance as the operating fluid for the system is an important criterion. However, the data in the figure show that the performance of most refrigerant mixtures does not have a performance advantage over one of their own components. The maximum  $COP_h$  of the refrigerant mixture (3.33) occurs at (R3, R4). From a long-term

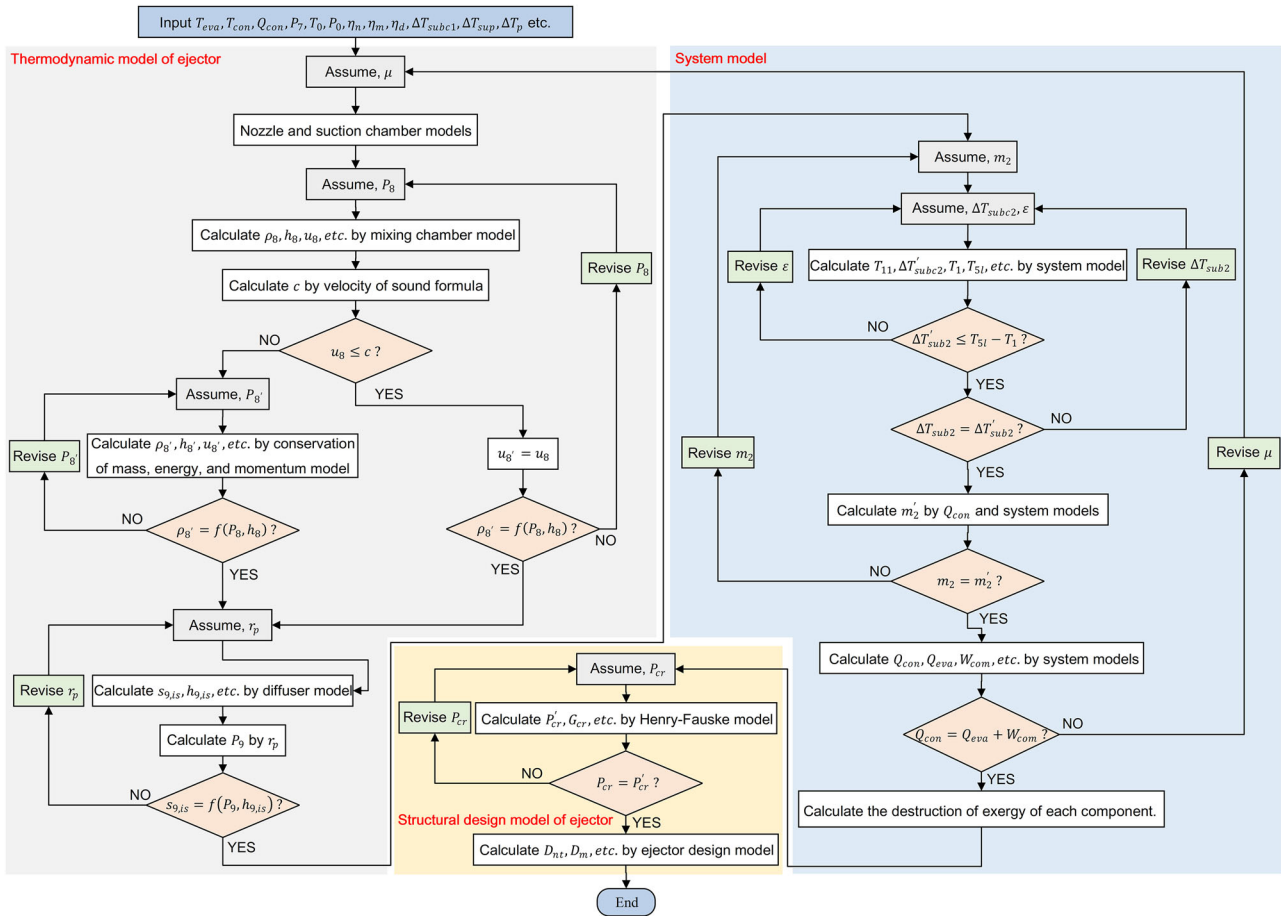


**Fig. 3 | Flowchart of system simulation calculation.** The calculation flowchart of the system can be divided into three parts, namely the thermodynamic model calculation of the ejector, the system model calculation, and the structural design calculation of the ejector.

**Table 6 | Physical properties and performance of refrigerants (order of boiling points)**

Number	Refrigerant	$t_b / (^{\circ}\text{C})$	$t_c / (^{\circ}\text{C})$	$L_v / (\text{kJ/kg}) (t = 100^{\circ}\text{C})$	GWP	$COP_h$	$\mu$
R1	R365mfc	40.09	186.86	154.04	804	3.35	1.02
R2	R1336mzz(Z)	33.45	171.35	127.07	<10	3.29	0.97
R3	R245ca	25.26	174.42	154.66	716	3.37	1.04
R4	R1233zd(E)	18.26	166.50	142.25	1	3.39	1.06
R5	R245fa	15.10	154.00	135.59	1030	3.21	0.94
R6	R1224yd(Z)	14.62	155.50	117.12	<1	3.24	0.95
R7	R1234ze(Z)	9.73	150.10	144.44	<1	3.28	0.99
R8	R236ea	6.19	139.29	102.32	1200	2.89	0.84
R9	R600	-0.60	153	258.26	0.1	3.22	0.97

application perspective, R3 (R245ca) is a high-GWP, non-environmentally-friendly refrigerant. Therefore, it is more reasonable to choose the refrigerant mixture (R4, R6) with the second-highest  $COP_h$  (3.32). In addition, the entrainment ratio of the ejector is also one of the factors we consider. The combination of (R4, R7) has a slightly lower performance than (R4, R6) but has a higher entrainment ratio. From a short-term practical application perspective, R245fa, one of the most widely used refrigerants in high-temperature heat pumps, urgently needs to be replaced. Using R245fa-based refrigerant mixtures can reduce the use of R245fa. Meanwhile, to test the separation characteristics of the refrigerant mixture, the (R5, R9) combination was chosen. It has a large boiling point difference (15.7 °C), and its two components respectively have the characteristics of high boiling point and low latent heat, as well as low boiling point and high latent heat.

Therefore, it was selected as a potential ideal working fluid for the refrigerant composition regulation research in this paper. Therefore, the refrigerant combination of (R1, R9), which has the largest boiling point difference (40.69 °C) and meets the characteristics of the (R5, R9) combination, also has research significance.

Table 7 presents the further calculation results of the four refrigerants mentioned above. From the perspective of refrigerant properties, the low-boiling-point components in R600/R245fa and R600/R365mfc exhibit relatively high latent heat of vaporization, with remarkable differences in both boiling points and latent heat of vaporization (as shown in Table 7), which are expected to provide a considerable range for composition regulation. In the R1224yd(Z)/R1233zd(E), the difference in latent heat of vaporization is greater than the difference in boiling points. Notably, the

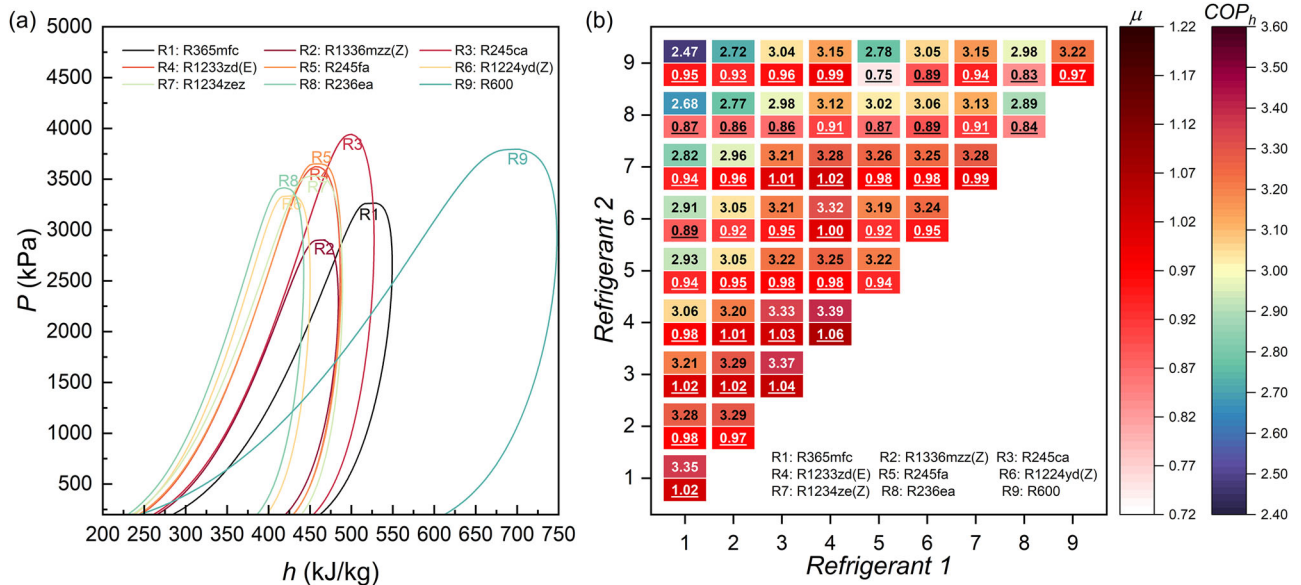


Fig. 4 | Refrigerant characteristics. a Pressure–enthalpy diagrams; b performance of pure refrigerants and mixtures.

Table 7 | Calculation results for two typical refrigerant mixtures

Refrigerant mixtures	$COP_h$	$\mu$	$m_{pf}$	$\eta_{eje}(\%)$	$m_2$	$z_{5l}$	$z_5$	$\Delta t_b$	$\Delta L_v$
R600/R245fa	2.78	0.75	0.35	36.02	0.84	0.54	0.5	15.7	122.67
R600/R365mfc	2.42	0.95	0.29	34.96	0.61	0.41	0.5	40.7	104.22
R1224yd(Z)/R1233zd(E)	3.32	0.99	0.46	44.65	0.91	0.49	0.5	3.7	25.13
R1234ze(Z)/R1233zd(E)	3.28	1.00	0.40	43.82	0.80	0.488	0.5	8.5	2.19

low-boiling-point component R1224yd(Z) has a latent heat of vaporization of 117.12 kJ/kg, which is lower than that of the high-boiling-point component. The R1234ze(Z)/R1233zd(E) mixture has a relatively small difference in latent heat of vaporization, only 2.19 kJ/kg, and its boiling point difference is also not remarkable. From the operational characteristics, except for R600/R245fa, the decrease in  $z_{5l}$  relative to  $z_5$  for the other three refrigerant mixtures ranges from 2.2% to 18.6%. This indicates that the low-boiling-point component evaporates more in the gas–liquid separator 1, and the high-boiling-point refrigerant content in the liquid phase is dominant. In contrast, for R600/R245fa,  $z_{5l}$  increased by 8.6% compared to  $z_5$ , suggesting that the high-boiling-point component evaporates more, while the low-boiling-point component (R600) is dominant in the liquid phase. This appears to contradict the characteristic of low-boiling-point components being more easily evaporated. However, it is important to note that the latent heat difference for R600/R245fa is much greater than its boiling point difference, and the high latent heat of vaporization of R600 may hinder its evaporation. To further investigate the component separation characteristics of refrigerant mixtures and select efficient, environmentally friendly refrigerants, this study focuses on R600/R245fa, where the low boiling component has high latent heat, and R1233zd(Z)/R1233zd(E), where the high boiling component has high latent heat. At the same time, R245fa, a widely used high-temperature refrigerant, has a critical temperature and critical pressure similar to those of R600, making it a feasible option for the practical application of the findings of this study.

**Influence of the initial composition and high-pressure subcooling**

To further determine the ideal initial composition and adjustable range of the selected refrigerant mixtures, this study investigates the initial composition of two refrigerant mixtures, with results shown in Fig. 5a. As shown in Fig. 5a, with the increase in the initial composition, the  $D_{no}$  of R600/R245fa

exhibits a decreasing trend, while  $D_m$  first increases and then decreases, reaching its peak at  $Z_0 = 0.3$ .  $D_{nt}$  follows a trend of first decreasing and then increasing, with its lowest value occurring at  $Z_0 = 0.7$ . Under constant high-pressure subcooling, compressor inlet superheat, and injection pressure, changes in the initial concentration led to variations in the composition of the refrigerant mixture at the ejector inlet, ultimately affecting the structural design parameters of the ejector. Taking  $z_0 = 0.5$  as the reference, the fluctuation ranges of  $D_{nt}$ ,  $D_{no}$ , and  $D_m$  with the initial composition are  $-9.55\%$  to  $-3.18\%$ ,  $-5.76\%$  to  $-19.75\%$ , and  $-1.56\%$  to  $-18.36\%$ , respectively, with  $D_m$  being adjusted downward by less than 2%. If the initial injection concentration is reduced to 0.4, the adjustment range of  $D_m$  changes to  $-4.64\%$  to  $14.67\%$ , but this simultaneously limits the upward adjustment range of  $D_{nt}$  to less than 1% (0.78%). Conversely, increasing the initial injection concentration will lead to a further decrease in  $D_m$ . For R1224yd(Z)/R1233zd(E), the three key design parameters of the ejector gradually increase with increasing  $z_0$ , exhibiting an overall trend opposite to that of R600/R245fa. Taking  $Z_0 = 0.5$  as the reference, the variation ranges of  $D_{nt}$ ,  $D_{no}$ , and  $D_m$  are  $-4.34\%$  to  $4.10\%$ ,  $-1.65\%$  to  $2.79\%$ , and  $-0.11\%$  to  $1.19\%$ , respectively, with the downward adjustment of  $D_m$  being only 0.11%. At this point, if the initial injection concentration is increased to 0.6, the adjustment range of  $D_m$  becomes  $-0.25\%$  to  $10.48\%$ , representing a relative increase of 0.15%, while the decrease in  $COP_h$  is 0.3%. To balance the adjustment range and performance of the initial concentration for the two refrigerant mixtures, this study adopts  $Z_0 = 0.5$  as the baseline for further investigation of the regulation capabilities of the two refrigerant mixtures.

Adjustments to system parameters not only affect the structure of the ejector but also influence the system’s performance. Consequently, Supplementary Notes 2–5 investigate the impact of initial concentration, high-pressure subcooling, superheat, and injection pressure on the system’s performance.

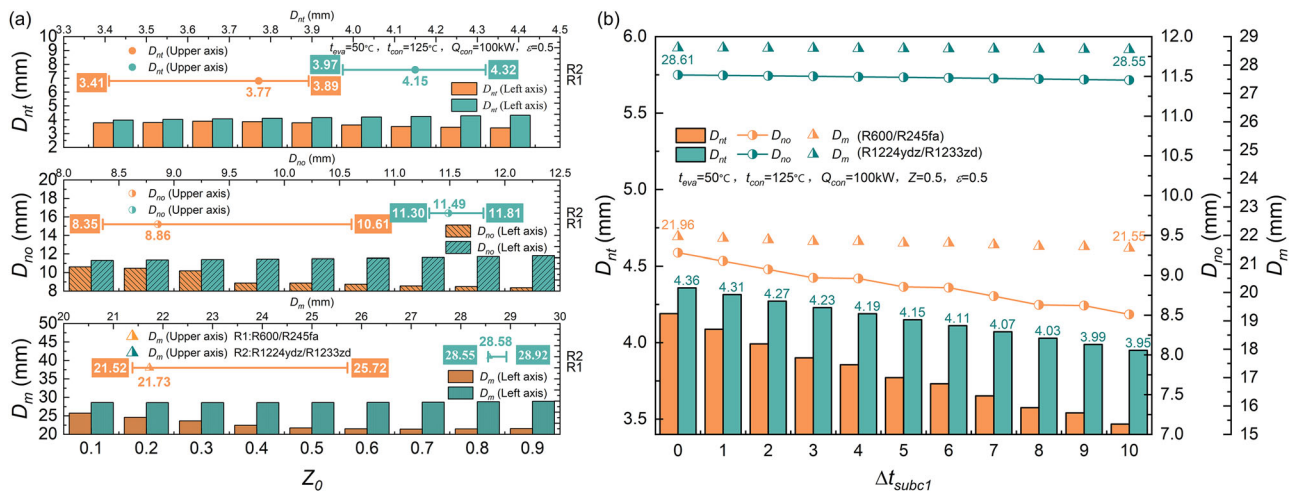


Fig. 5 | Effect of system operating parameters on the structural parameters of the ejector. a Initial composition; b High-pressure subcooling.

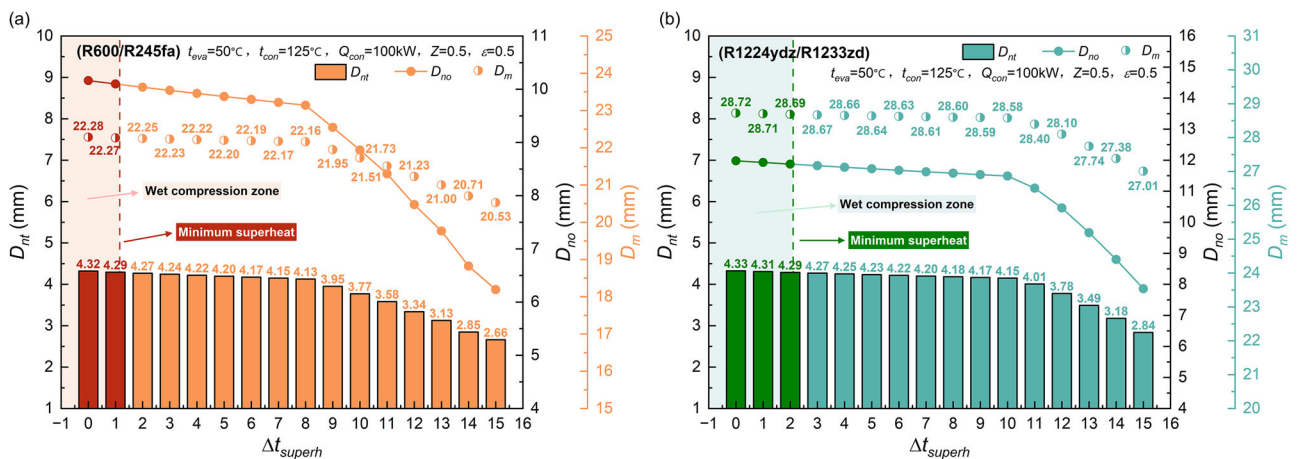


Fig. 6 | Effect of compressor inlet superheat on the structural parameters of the ejector. a R600/R245fa; b R1224yd(Z)/R1233zd(E).

High-pressure subcooling, compressor inlet superheat, and injection pressure are key parameters affecting system performance and the design values of the ejector structure, and they exhibit a certain degree of variability. In the system discussed in this paper, these three parameters play a crucial role in regulating the inlet and outlet states of the ejector as well as the composition of the refrigerant. This part investigates the impact of high-pressure subcooling on system performance and the ejector’s structural design parameters, with the calculation results shown in Fig. 5b. As shown in Fig. 5b, for both refrigerant mixtures, an increase in subcooling simultaneously leads to a reduction in the three key dimensions of the ejector. Taking a subcooling of 5 °C as the baseline, the adjustment ranges of  $D_{nt}$ ,  $D_{no}$ , and  $D_m$  for R600/R245fa are  $-8.07\%$  to  $11.09\%$ ,  $-3.91\%$  to  $4.81\%$ , and  $-0.84\%$  to  $1.05\%$ , respectively; while for R1224yd(Z)/R1233zd(E), the corresponding ranges are  $-4.82\%$  to  $5.03\%$ ,  $-0.31\%$  to  $0.26\%$ , and  $-0.12\%$  to  $0.09\%$ . In terms of subcooling regulation, R600/R245fa exhibits a wider adjustment range than R1224yd(Z)/R1233zd(E), with a particular advantage in adjusting  $D_{nt}$ .

**The adjustable range of the compressor inlet superheat**

For high-temperature heat pumps, the selected refrigerants are all considered wet refrigerants (as defined by Yu et al.<sup>36</sup>), and a certain degree of superheat is required at the compressor inlet to prevent the compression process from entering the two-phase region. Figure 6 shows the three key design dimensions of the ejector for R600/R245fa and R1224yd(Z)/

R1233zd(E) under different compressor inlet superheat conditions. Taking 10 °C as the reference baseline, the adjustment ranges of  $D_{nt}$ ,  $D_{no}$ , and  $D_m$  for R600/R245fa are  $-29.45\%$  to  $13.20\%$ ,  $-29.58\%$  to  $13.36\%$ , and  $-5.53\%$  to  $2.39\%$ , respectively; for R1224yd(Z)/R1233zd(E), the corresponding adjustment ranges for  $D_{nt}$ ,  $D_{no}$ , and  $D_m$  are  $-31.61\%$  to  $2.91\%$ ,  $-31.61\%$  to  $2.91\%$ , and  $-5.49\%$  to  $0.32\%$ , respectively. Compressor inlet superheat is advantageous for adjusting  $D_{nt}$  and  $D_{no}$ , but the upward adjustment capability for both refrigerant mixtures is insufficient, particularly for R1224yd(Z)/R1233zd(E).

**The adjustable range of injection pressure**

Due to differences in evaporation and condensation pressures among various refrigerants and the pressure boosting characteristics of the ejector, the range of intermediate injection pressures in the compressor also varies. As shown in Fig. 7a, the  $D_{nt}$  and  $D_{no}$  of both refrigerant mixtures are minimally affected by changes in injection pressure. Compared to the design parameters at the baseline injection pressure, the adjustment ranges of  $D_{nt}$  and  $D_{no}$  for R600/R245fa under different injection pressure are  $-5.69\%$  to  $9.35\%$  and  $-5.69\%$  to  $4.56\%$ , respectively; for R1224yd(Z)/R1233zd(E), the adjustment ranges for both  $D_{nt}$  and  $D_{no}$  are  $-3.98\%$  to  $-0.05\%$ . Figure 7b displays the trend of the ejector mixing chamber diameter ( $D_m$ ) for the two refrigerant mixtures under different injection pressures. It can be observed that  $D_m$  follows the same trend as  $COP_h$ , with R600/R245fa reaching a maximum  $D_m$  of 22.20 mm at an intermediate pressure of 1800kPa, and

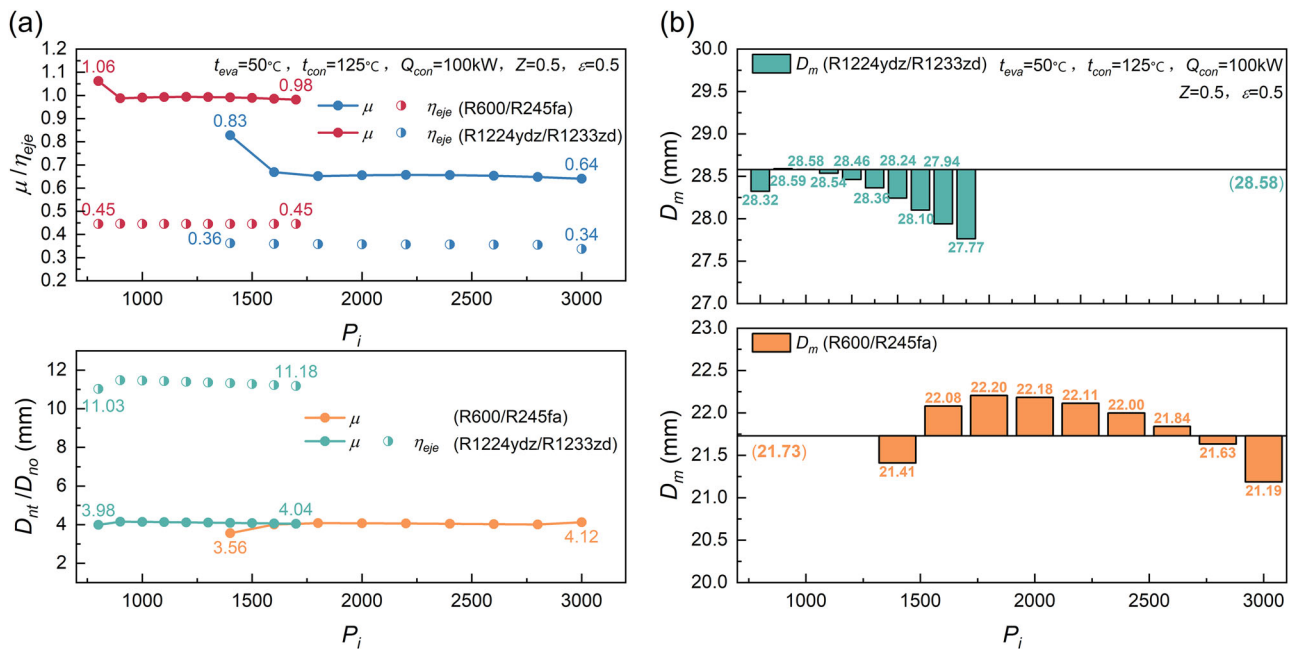


Fig. 7 | The impact of compressor discharge pressure on the ejector. **a** Structure; **b** performance.

R1224yd(Z)/R1233zd(E) achieving a maximum  $D_m$  of 28.59 mm at an intermediate pressure of 900 kPa. Compared to the mixing chamber diameter ( $D_m$ ) calculated at the reference injection pressure, the variation ranges of  $D_m$  for R600/R245fa and R1224yd(Z)/R1233zd(E) under different injection pressures are  $-2.50\%$  to  $2.08\%$  and  $-2.85\%$  to  $0.04\%$ , respectively. Overall, the injection pressure has a minimal effect on the adjustment of ejector design dimensions, particularly on the mixing chamber diameter.

### Flow rate changes in the primary fluid

The preceding content elucidated the adjustable ranges of three parameters concerning various structural aspects of the ejector. This section will investigate the design values of ejector structures under varying condenser heating capacity, corresponding to different primary flow rates of the ejector. Simultaneously, by comparing the adjustable ranges of the aforementioned parameters with the design value ranges under fluctuating operating conditions, appropriate parameter adjustment methods are selected. Figure 8 depicts the fluctuation ranges of ejector structural parameter design values and the adjustment ranges of tunable parameters for R600/R245fa and R1224yd(Z)/R1233zd(E) under different condenser heating capacities. As shown in Fig. 8a, the left side illustrates the design values of ejector structural parameters under varying condenser heating capacity. When the condenser heat release fluctuates within the range of  $-5\%$  to  $5\%$ , the design values of ejector structural parameters increase or decrease accordingly, exhibiting a positive correlation. For R600/R245fa, the fluctuation ranges for  $D_{nt}$ ,  $D_{no}$ , and  $D_m$  are  $-2.55\%$  to  $2.47\%$ ,  $-2.58\%$  to  $2.47\%$ , and  $-2.50\%$  to  $2.47\%$ , respectively. The right side of Fig. 8a illustrates the adjustable ranges of three key structural parameters when individually tuning each parameter; the specific variation ranges have been introduced earlier. This section focuses on comparing the fluctuation ranges of the ejector structural parameter design values with their adjustable ranges. For  $D_{nt}$  and  $D_{no}$ , the adjustable ranges of the three tunable parameters can cover the fluctuation ranges due to load variations. Specifically, the adjustment range of subcooling exceeds the upper and lower fluctuation limits of  $D_{nt}$  by  $8.55\%$  and  $5.71\%$ , respectively, and exceeds those of  $D_{no}$  by  $2.32\%$  and  $1.39\%$ . The adjustment range of compressor inlet superheat exceeds the upper and lower fluctuation limits of  $D_{nt}$  by  $10.62\%$  and  $27.72\%$ , respectively, and exceeds those of  $D_{no}$  by  $10.69\%$  and  $27.69\%$ . The adjustment range of injection pressure exceeds the upper and lower fluctuation limits of  $D_{nt}$  by  $6.74\%$  and  $3.26\%$ , respectively, and exceeds those of  $D_{no}$  by  $5.51\%$  and

$3.24\%$ . However, for the adjustment of  $D_m$ , subcooling regulation cannot effectively cover the load fluctuation range; the lower limit of superheating regulation exceeds the load fluctuation requirement by  $3.11\%$ , while the upper limit is  $0.09\%$  lower than the fluctuation upper limit; the adjustment lower limit of the injection pressure is the same as the fluctuation lower limit, and the upper limit is  $0.23\%$  lower than the fluctuation upper limit. The adjustment ranges of the three adjustable parameters still have slight differences in covering the fluctuation range of  $D_m$ . Considering the impact of correction errors ( $1\%$ ), both superheating and injection pressure adjustments can meet the regulation requirements for load fluctuations.

Figure 8b illustrates the fluctuation ranges of the ejector structural design parameters  $D_{nt}$ ,  $D_{no}$ , and  $D_m$  resulting from the heating capacity of R1224yd(Z)/R1233zd(E). The fluctuations are  $-2.65\%$  to  $2.41\%$ ,  $-2.51\%$  to  $2.45\%$ , and  $-2.55\%$  to  $2.45\%$ , respectively. The right side of Fig. 8b indicates that the three adjustable parameters for R1224yd(Z)/R1233zd(E) exhibit limited adjustability, especially concerning the upper adjustment limits. For high-pressure subcooling, it only shows an advantage in adjusting  $D_{nt}$ , with upper and lower adjustment limits exceeding fluctuation limits by  $2.59\%$  and  $2.23\%$ , respectively. Superheating demonstrates advantages in adjusting both  $D_{nt}$  and  $D_{no}$ , with upper and lower adjustment limits exceeding fluctuation limits by  $0.47\%$  and  $29.70\%$  for  $D_{nt}$ , and  $0.42\%$  and  $29.82\%$  for  $D_{no}$ . Injection pressure has an advantage in the lower adjustment limit, but its upper adjustment limits are lower than fluctuation limits by  $2.35\%$ ,  $2.46\%$ , and  $5.77\%$  for  $D_{nt}$ ,  $D_{no}$ , and  $D_m$ , respectively. Therefore, in terms of the adjustable range for load fluctuation control in R1224yd(Z)/R1233zd(E), the adjustment upper limit of injection pressure is insufficient to achieve the desired  $\pm 5\%$  load fluctuation control. It is important to note that the ejector structural parameters discussed in this and the previous section are design parameters, representing the calculated values under specific conditions (such as certain superheat or subcooling degrees). These parameters are used to evaluate the adjustment capabilities (impact ranges) of different adjustable parameters on the three key structural parameters of the ejector.

From the perspective of adjustable parameters, the high-pressure subcooling degree satisfies the regulation requirements of  $D_{nt}$  and  $D_{no}$  for R600/R245fa, but only fulfills the  $D_{nt}$  regulation requirements for R1224yd(Z)/R1233zd(E). The superheat degree meets the regulation requirements of  $D_{nt}$  and  $D_{no}$  for both R600/R245fa and R1224yd(Z)/R1233zd(E). Meanwhile, the injection pressure, within the allowable error range, can address the  $D_m$  regulation requirements for R600/R245fa, but

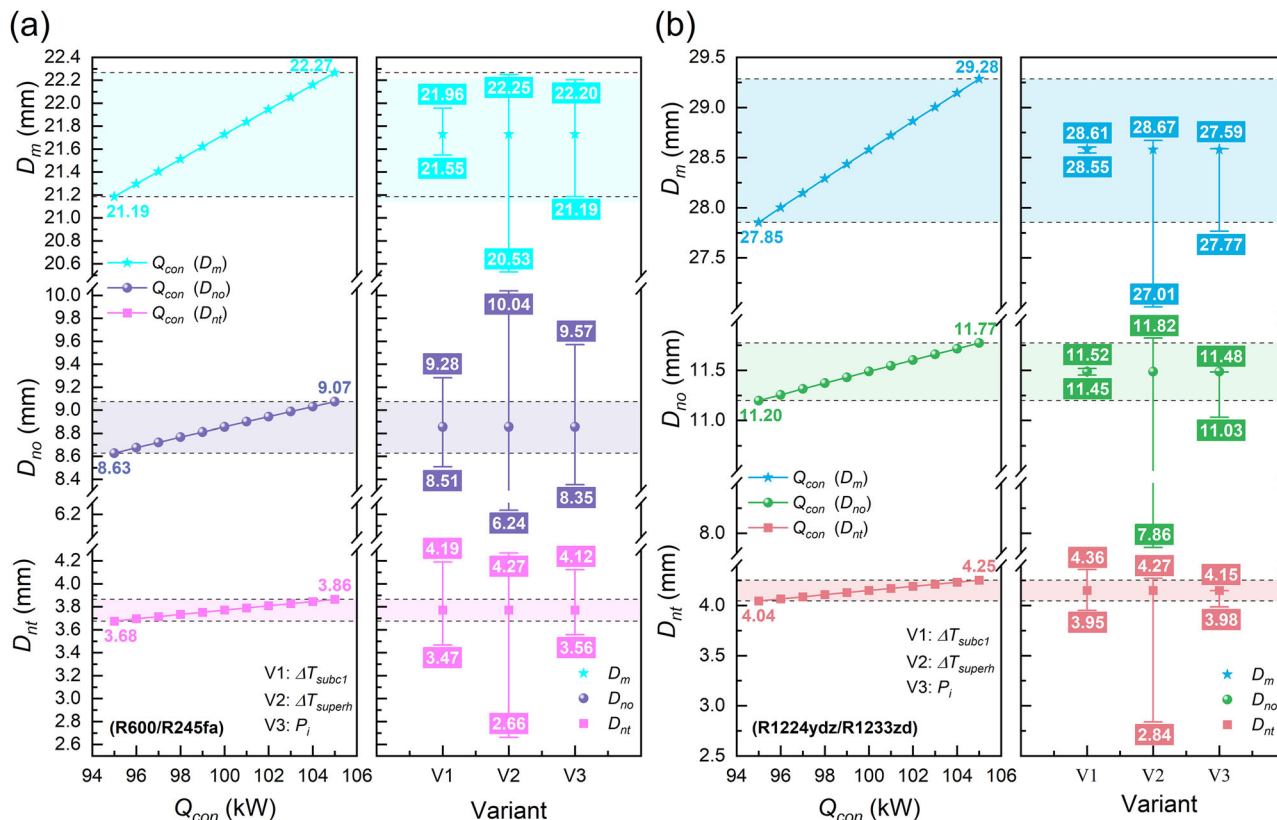


Fig. 8 | Comparison of the fluctuation range and adjustable range of the ejector. a R600/R245fa; b R1224yd(Z)/R1233zd(E).

fails to reach the upper regulation limits for the three parameters ( $D_{nt}$ ,  $D_{no}$ ,  $D_m$ ) in R1224yd(Z)/R1233zd(E).

### Component adjustment of refrigerant mixtures

In practical applications, ejectors typically have fixed structures, making it challenging to adjust their design parameters in response to load fluctuations. Although adjustable ejectors have been proposed to address this issue, they still face numerous challenges, and further research is ongoing. When an ejector operates under varying primary fluid flow rate conditions, structural mismatches can lead to a 25%–30% performance decline, and in severe cases, may result in operational failure. Therefore, this section explores adjusting three controllable parameters to modify the refrigerant mixture composition at the ejector’s inlet and outlet, thereby correcting the ejector’s structural parameters to their design values. For example, if a 100 kW heating load decreases to 95 kW, the design value of  $D_{nt}$  for an R600/R245fa ejector changes from 3.77 mm to 3.68 mm. Since the actual ejector’s  $D_{nt}$  remains at 3.77 mm and cannot be altered accordingly, adjusting the three controllable parameters (subcooling degree, superheat degree, and economizer pressure) can change the refrigerant mixture composition at the ejector’s inlet and outlet, correcting the deviation caused by load fluctuations (3.77 mm → 3.68 mm) back to the actual ejector’s structural dimension (3.68 mm → 3.77 mm).

Figure 9 illustrates the effects of high-pressure subcooling, superheat, and injection pressure on the regulation of key parameters in R600/R245fa systems, along with their respective adjustment ranges. In Fig. 9a, each small square represents a specific operating condition, i.e., different condenser heating capacity. Within each square, the vertical axis denotes the value of  $D_{nt}$ , while the horizontal axis indicates the level of high-pressure subcooling. The central horizontal solid line within each square represents the reference  $D_{nt}$  value ( $D_{nt} = 3.77$  mm) based on a 100 kW baseline, and the central vertical dashed line indicates the baseline high-pressure subcooling ( $\Delta T_{subc1} = 5$  °C). When the condenser heating capacity decreases from 100 kW to 95 kW, the design value of the ejector’s  $D_{nt}$  shifts from 3.77 mm

to 3.68 mm, as depicted in the first small square of Fig. 9a. At this point, the design value of  $D_{nt}$  corresponds to the vertical coordinate at the lower boundary of the pink rectangular block. By reducing the baseline subcooling from 5 °C to 3.7 °C, the composition of the refrigerant mixture at the ejector’s inlet and outlet changes, adjusting the design value of  $D_{nt}$  back to the vertical coordinate at the upper boundary of the pink rectangular block, i.e., the reference  $D_{nt}$  value. This adjustment corrects the deviation in the design value caused by load fluctuations, enabling the fixed-geometry ejector to adapt to varying operating conditions. The vertical length of the pink rectangular block represents the range of correction for the  $D_{nt}$  design value, while the horizontal length indicates the adjustment span of the high-pressure subcooling. It’s important to note that changes in subcooling not only affect the design value of  $D_{nt}$  but also influence the design values of  $D_{nt}$  and  $D_m$ . Similarly, the correction of the  $D_{nt}$  design value here is not solely the result of high-pressure subcooling; rather, it is the combined effect of all three adjustable parameters. This differs from previous sections. In this section, the joint action of the three parameters achieves the adjustment of refrigerant mixture composition under certain operating conditions.

From the results, as the fluctuation amplitude of the condenser heat release increases, the correction amounts of  $D_{nt}$ ,  $D_{no}$ , and  $D_m$  in the R600/R245fa system also increase, and the adjustment ranges of the controllable parameters correspondingly expand. Specifically: The adjustment range of  $\Delta T_{subc1}$  is from 3.7 °C to 6.4 °C; The adjustment range of  $\Delta T_{superh}$  is from 9.7 °C to 10.55 °C; The adjustment range of  $P_i$  is from 1385.6 kPa to 1585.6 kPa. Notably, when the condenser heat release is 100 kW, adjusting the high-pressure subcooling degree, superheat degree, and vapor injection pressure to 5.9 °C, 10.25 °C, and 1535.6 kPa, respectively, can achieve the same design values of  $D_{nt}$ ,  $D_{no}$ , and  $D_m$ . This phenomenon arises from the combined effects of the three adjustable parameters and correction errors. Therefore, in joint regulation, the sequence and method of adjusting different parameters are not unique. Additionally, variations in high-pressure subcooling degree, superheat degree, and injection pressure themselves impact the performance of the system and ejector.

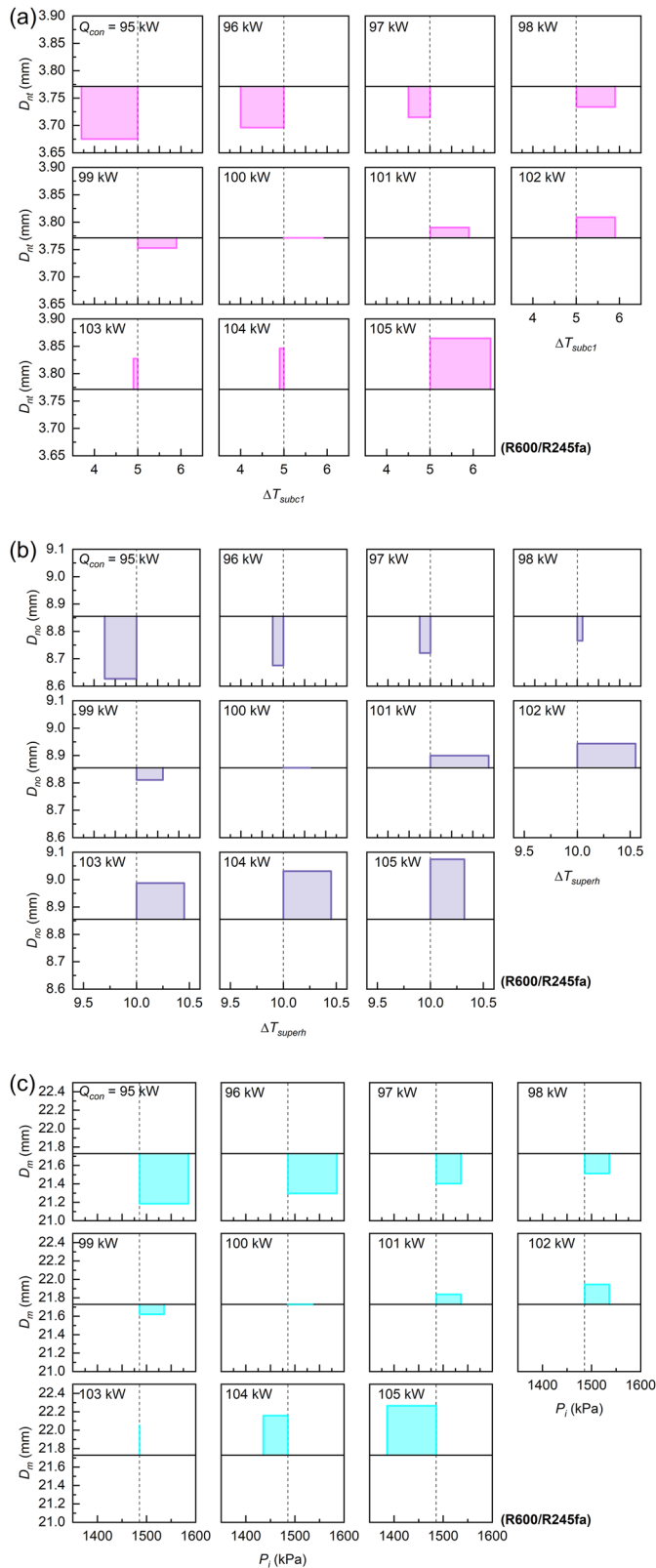


**Fig. 9 | Adjustment of compressor injection pressure and corresponding change in the structure of the ejector for each load (R600/R245fa). a** Nozzle throat diameter; **b** nozzle outlet diameter; **c** mixing chamber diameter.

For R1224yd(Z)/R1233zd(E), the limited upper adjustment capacity of the three adjustable parameters for  $D_m$  makes it challenging to meet the variable load regulation requirements. When the condenser heating capacity decreases, the design value of  $D_m$  correspondingly decreases. To correct

the design value of  $D_m$ , an upward adjustment is necessary. However, the upward adjustment range of injection pressure for  $D_m$  is only 0.84%. Therefore, when the condenser heat release decreases to 97 kW, the combined parameter adjustment cannot correct the design values of the ejector’s structural parameters due to the limited upward adjustment capability for  $D_m$ . As shown in Fig. 10, the combined control patterns for R1224yd(Z)/R1233zd(E) are similar to those for R600/R245fa, with  $\Delta T_{subc1}$  ranging from 4.9 °C to 6.6 °C,  $\Delta T_{superh}$  ranging from 10 °C to 10.7 °C, and  $P_i$  ranging from 800 kPa to 900 kPa. At 100 kW, adjusting the high-pressure subcooling, superheat, and suction pressure to 4.9 °C, 10 °C, and 850 kPa, respectively, can achieve the same design values for the ejector’s structural parameters as the reference parameters.

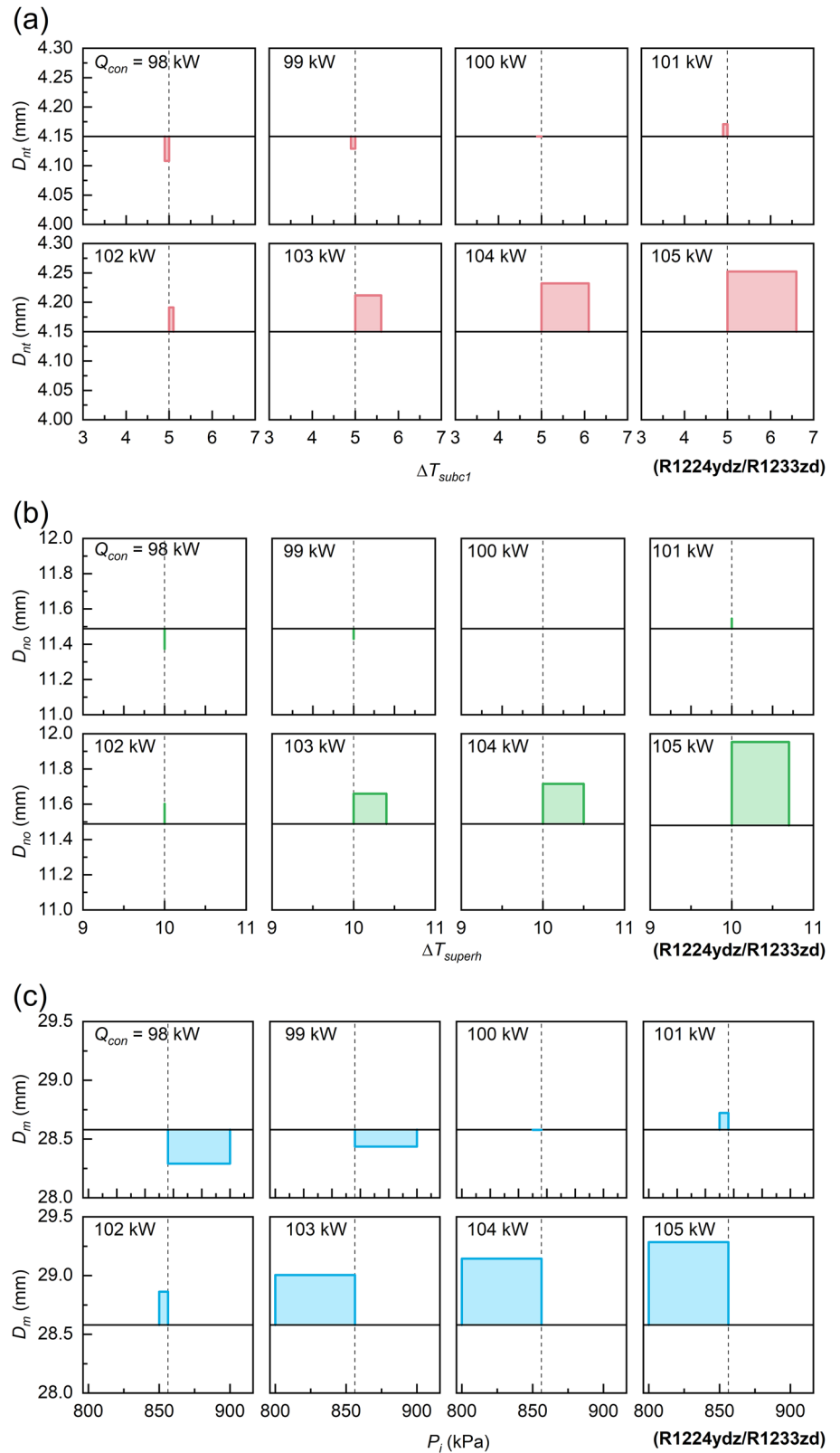
### Conclusions

To address the challenges faced by ejectors under variable loads, this study proposes a novel approach to correct deviations in ejector structural parameter design values by adjusting the composition of refrigerant mixtures. A parameter-adjustable high-temperature heat pump system is modeled to evaluate the regulation capabilities of key parameters. The study also introduces and elaborates on the concept of equivalent ejector efficiency. The results show that the proposed concept offers a promising alternative for advancing industrial waste heat recovery using high-temperature heat pumps with ejectors under fluctuating load conditions. Several key findings are summarized as follows:

1. The saturation vapor line of high-critical-temperature refrigerants exhibits a positive slope, resulting in issues such as insufficient vapor quality at the vapor injection separation point and compression processes entering the two-phase region. The novel system design in this study addresses these challenges by enhancing separation vapor quality through subcooling heat utilization, while simultaneously fulfilling the minimum superheat requirement.
2. In the R600/R245fa mixture, R600 (with a low boiling point and high latent heat of vaporization) dominates the composition on the evaporator side, whereas R245fa (with a higher boiling point) demonstrates greater evaporation propensity. The evaporation separation characteristics of refrigerant mixtures are governed by both boiling point and latent heat of vaporization, rather than being exclusively dependent on boiling point.
3. For R600/R245fa, the maximum adjustment capabilities of high-pressure subcooling, superheat, and vapor injection pressure are observed in  $D_{nt}$  (−8.07% to 11.09%),  $D_{no}$  (−29.58% to 13.36%), and  $D_m$  (−5.69% to 9.35%), respectively. In R1224yd(Z)/R1233zd(E), the maximum adjustment capabilities of these three parameters occur in  $D_{nt}$  (−4.82%~5.03%),  $D_{nt}/D_{no}$  (−29.58%~13.36%), and  $D_{nt}/D_{no}$  (−3.98%~0.05%), respectively.
4. Under load fluctuations of −5% to 5%, the three adjustable parameters fail to meet the upper  $D_m$  regulation threshold for R1224yd(Z)/R1233zd(E). Even the superheat degree, which exhibits the highest adjustability, still falls short by 2.08%. For R600/R245fa, the maximum  $D_m$  adjustability of superheat degree is 0.09% lower than the upper load fluctuation limit. Considering comprehensively, the high-pressure subcooling, superheat, and intermediate pressure are respectively responsible for adjusting  $D_{nt}$ ,  $D_{no}$ , and  $D_m$ .
5. For R1224yd(Z)/R1233zd(E), the lower limit of actual load fluctuation is 98 kW, and the three adjustable parameters demonstrate joint regulation behavior, where the sequence of adjustment and error correction methods is non-unique. For R600/R245fa, the  $COP_h$  and  $\eta_{ejc}$  vary within −1.18% to 0.96% and −2.49% to 1.19%, respectively, post-regulation. For R1224yd(Z)/R1233zd(E), these ranges are −0.58% to 0.27% ( $COP_h$ ) and −0.13% to 0.77% ( $\eta_{ejc}$ ) (From Supplementary Note 6).

According to the research results of this paper, the greater the difference in boiling points and latent heat of vaporization among the components of the refrigerant mixture, the wider the adjustable load range.

**Fig. 10 | Adjustment of compressor injection pressure and corresponding change in the structure of the ejector for each load (R1224yd(Z)/R1233zd(E)). a** Nozzle throat diameter; **b** nozzle outlet diameter; **c** mixing chamber diameter.



However, due to the high-temperature characteristics of high-temperature heat pumps and limitations imposed by environmental factors, the selection of working fluids is somewhat restricted. Further in-depth research is needed on the separation of different components within the refrigerant mixture itself. In addition, the method of cycle equivalence analysis provides a new perspective for analyzing the impact of refrigerant mixture component migration on the system, but this study is very limited in this regard.

**Data availability**

The datasets generated and/or analyzed during the current study are available within the paper. Other materials and data are available from the corresponding author, Youcai Liang, upon reasonable request.

Received: 13 April 2025; Accepted: 22 September 2025;

Published online: 12 November 2025

## References

- Energy institute: Statistical Review of World Energy, 2024. <https://www.energyinst.org/statistical-review> (2025).
- International Energy Agency: CO2 Emissions in 2023, 2023. <https://www.iea.org/reports/co2-emissions-in-2023> (2024).
- Leonzio, G. & Shah, N. Recent advancements and challenges in carbon capture, utilization and storage. *Curr. Opin. Green Sustain. Chem.* **46**, 100895 (2024).
- Liu, Z. et al. Global carbon emissions in 2023. *Nat. Rev. Earth Environ.* **5**, 253–254 (2024).
- Liang, Y. et al. Energy consumption optimization of CO2 capture and compression in natural gas combined cycle power plant through configuration modification and process integration. *Appl. Therm. Eng.* **255**, 124019 (2024).
- El Samad, T. et al. A review of compressors for high temperature heat pumps. *Therm. Sci. Eng. Prog.* **51**, 102603 (2024).
- Sadeghi, M. et al. Thermal and economic performance assessment of different high temperature heat pump layouts for upgrading district heating to & process heating of steam production at 160 °C. *Energy* **313**, 133832 (2024).
- Dong, Y. et al. High temperature heat pump with dual uses of cooling and heating for industrial applications. *Appl. Energy* **379**, 124962 (2025).
- Yang, L. et al. Operating characterization and performance optimization of high-temperature heat pumps: a comparative energy, economic and environmental analysis. *Appl. Therm. Eng.* **257**, 124292 (2024).
- Wang, J. et al. The effectiveness of vapor-injection for an inverter air-source heat pump compared with vapor-return. *Appl. Therm. Eng.* **245**, 122827 (2024).
- Xu, X., Hwang, Y. & Radermacher, R. Refrigerant injection for heat pumping/air conditioning systems: literature review and challenges discussions. *Int. J. Refrig.* **34**, 402–415 (2011).
- Feng, C. et al. Thermodynamic analysis of a dual-pressure evaporation high-temperature heat pump with low GWP zeotropic mixtures for steam generation. *Energy* **294**, 130964 (2024).
- Cui, C. et al. Energy and economic analysis of a sub-cooler based vapor injection transcritical CO2 heat pump for space heating. *Int. J. Refrig.* **159**, 241–253 (2024).
- Wang, J. et al. The difference between vapor injection cycle with flash tank and intermediate heat exchanger for air source heat pump: An experimental and theoretical study. *Energy* **221**, 119796 (2021).
- Li, H. et al. Thermo-economic performance of geothermal driven high-temperature flash tank vapor injection heat pump system: a comparison study. *Energy Eng.* **120**, 1817–1835 (2023).
- Sarkar, J. Ejector enhanced vapor compression refrigeration and heat pump systems—a review. *Renew. Sustain. Energy Rev.* **16**, 6647–6659 (2012).
- Geng, L. *Study on Bi-Evaporator Compression/Ejection Refrigeration System and Two-Phase Ejector* (Zhengzhou University, Zhengzhou, 2017). (in Chinese).
- Fingas, R. et al. Experimental analysis of the air-to-water ejector-based R290 heat pump system for domestic application. *Appl. Therm. Eng.* **236**, 121800 (2024).
- Mateu-Royo, C. et al. Theoretical performance evaluation of ejector and economizer with parallel compression configurations in high temperature heat pumps. *Int. J. Refrig.* **119**, 356–365 (2020).
- Jing, S., Chen, Q. & Yu, J. Analysis of an ejector-assisted flash tank vapor injection heat pump cycle with dual evaporators for dryer application. *Energy* **286**, 129531 (2024).
- Liang, Y. et al. Thermodynamic and economic analysis of a novel solar-assisted vapor injection ejector-enhanced cycle for building heating. *Int. J. Refrig.* **169**, 346–361 (2025).
- Ceylan, H. Review on the two-stage vapor injection heat pump with a flash tank. *Eng. Sci. Technol., Int. J.* **48**, 101583 (2023).
- Xu, X., Hwang, Y. & Radermacher, R. Transient and steady-state experimental investigation of flash tank vapor injection heat pump cycle control strategy. *Int. J. Refrig.* **34**, 1922–1933 (2011).
- Wang, X. et al. Experimental investigation of a double-slider adjustable ejector under off-design conditions. *Appl. Therm. Eng.* **196**, 117343 (2021).
- Banasiak, K. et al. Development and performance mapping of a multi-ejector expansion work recovery pack for R744 vapor compression units. *Int. J. Refrig.* **57**, 265–276 (2015).
- Al-Doori, G. et al. A review of axial and radial ejectors: geometric design, computational analysis, performance, and machine learning approaches. *Appl. Therm. Eng.* **266**, 125694 (2025).
- Liu, F. et al. Transient numerical study of CO2 two-phase flow in a needle adjustable ejector. *Int. J. Heat. Mass Transf.* **214**, 124395 (2023).
- Shahzamanian, B. et al. Performance evaluation of a variable geometry ejector applied in a multi-effect thermal vapor compression desalination system. *Appl. Therm. Eng.* **195**, 117177 (2021).
- Chen, J., Yu, J. & Qian, S. Subcooling control method for the adjustable ejector in the direct expansion solar assisted ejector-compression heat pump water heater. *Appl. Therm. Eng.* **148**, 662–673 (2019).
- Wang, R. et al. High temperature heat pumps for industrial heating processes using water as refrigerant. *Energy* **313**, 133847 (2024).
- Ma, X. et al. A comprehensive review of compression high-temperature heat pump steam system: status and trend. *Int. J. Refrig.* **164**, 218–242 (2024).
- Jiang, J. et al. A review and perspective on industry high-temperature heat pumps. *Renew. Sustain. Energy Rev.* **161**, 112106 (2022).
- Obika, E., Heberle, F. & Brüggemann, D. Thermodynamic analysis of novel mixtures including siloxanes and cyclic hydrocarbons for high-temperature heat pumps. *Energy* **294**, 130858 (2024).
- Brodal, E. & Eiksund, O. Optimization study of heat pumps using refrigerant blends—rjector versus expansion valve systems. *Int. J. Refrig.* **111**, 136–146 (2020).
- Ganesan, P. & Eikevik, T. M. New zeotropic CO2-based refrigerant mixtures for cascade high-temperature heat pump to reach heat sink temperature up to 180 °C. *Energy Convers. Manag. X* **20**, 100407 (2023).
- Yu, Z. & Ouderji, Z. H. A unified approach for the thermodynamic comparison of heat pump cycles. *Commun. Eng.* **2**, 62 (2023).
- Elbel, S. & Hrnjak, P. Experimental validation of a prototype ejector designed to reduce throttling losses encountered in transcritical R744 system operation. *Int. J. Refrig.* **31**, 411–422 (2008).
- Mateu-Royo, C. et al. Thermodynamic analysis of low GWP alternatives to HFC-245fa in high-temperature heat pumps: HCFO-1224yd (Z), HCFO-1233zd (E) and HFO-1336mzz (Z). *Appl. Therm. Eng.* **152**, 762–777 (2019).
- Henry, R. E. & Fauske, H. K. The two-phase critical flow of one-component mixtures in nozzles, orifices, and short tubes. *J. Heat. Transf.* **93**, 179–187 (1971).
- Liu, Q. Q. *Research on Performance of Air Source Heat Pump System for Alternate Defrosting with Supercooled Heat* (Nanjing University of Science & Technology, Nanjing, 2020). (in Chinese).
- Elbel, S. *Experimental and Analytical Investigation of a Two-Phase Ejector Used for Expansion Work Recovery in a Transcritical R744 Air-Conditioning System*. Ph.D. dissertation, University of Illinois at Urbana-Champaign (2007).
- Qi, D. Ejector design and energy-saving analysis of vapor compression/ejection refrigeration system. *J. Refrig.* **35**, 103–108 (2014). (In Chinese).
- Tang, B. K. *Study on Compression-Ejection Refrigeration System and Ejector* (Zhengzhou University, Zhengzhou, 2013). (in Chinese).
- Li, Z. et al. Theoretical study of a novel ejector-enhanced heat pump system with subcooling defrosting under cold conditions. *Energy Convers. Manag.* **326**, 119507 (2025).

## Acknowledgements

This research is supported by the National Natural Science Foundation of China (No. 52176006), Basic and Applied Basic Research Foundation of Guangdong Province (No. 2022A1515011496), Guangdong High-level Talent Project (No. 2021QN02L165), and the Fundamental Research Funds for the Central Universities (2024ZYGXZR019).

## Author contributions

Zhengyong Li originated the concept, derived the theoretical model, analyzed the simulation data, prepared the figures, and wrote the manuscript. Youcai Liang (Corresponding author) secured the funds, reviewed the paper, and supervised the project. Yan Zhu reviewed the paper and corrected parts of the content. Shunchun Yao supervised the project. Zhibin Yu reviewed the paper and corrected parts of the content.

## Competing interests

The authors declare no competing interests.

## Additional information

**Supplementary information** The online version contains supplementary material available at <https://doi.org/10.1038/s44172-025-00518-y>.

**Correspondence** and requests for materials should be addressed to Youcai Liang or Zhibin Yu.

**Peer review information** *Communications Engineering* thanks Yuyan Jiang, Zhenying Zhang, and Cong Guo for their contribution to the peer

review of this work. Primary Handling Editors: [Sunghoon Hur] and [Rosamund Daw]. [A peer review file is available].

**Reprints and permissions information** is available at <http://www.nature.com/reprints>

**Publisher's note** Springer Nature remains neutral with regard to jurisdictional claims in published maps and institutional affiliations.

**Open Access** This article is licensed under a Creative Commons Attribution-NonCommercial-NoDerivatives 4.0 International License, which permits any non-commercial use, sharing, distribution and reproduction in any medium or format, as long as you give appropriate credit to the original author(s) and the source, provide a link to the Creative Commons licence, and indicate if you modified the licensed material. You do not have permission under this licence to share adapted material derived from this article or parts of it. The images or other third party material in this article are included in the article's Creative Commons licence, unless indicated otherwise in a credit line to the material. If material is not included in the article's Creative Commons licence and your intended use is not permitted by statutory regulation or exceeds the permitted use, you will need to obtain permission directly from the copyright holder. To view a copy of this licence, visit <http://creativecommons.org/licenses/by-nc-nd/4.0/>.

© The Author(s) 2025